Supplementary Information for Sub-Diffraction Optical Confinement for Enhanced Second-Harmonic Generation in Suspended Thin-Film Lithium Niobate Nano-Cavity

Zengya Li[1,2,†], Zhuoran Hu[1,2,†], Weihao Wu[1,2], Guangfeng Wang[1,2], Hao Li[1,2], Shijie Liu[1,2], Bo Wang[1,2], Yuanlin Zheng[1,2,3,*], Xianfeng Chen[1,2,3,4,*]

[1]State Key Laboratory of Micro-Nano Engineering Science, School of Physics and Astronomy, Shanghai Jiao Tong University, Shanghai 200240, China.

[2]State Key Laboratory of Photonics and Communications, Shanghai Jiao Tong University, Shanghai 200240, China

[3]Shanghai Research Center for Quantum Sciences, Shanghai 201315, China.

[4]Collaborative Innovation Center of Light Manipulations and Applications, Shandong Normal University, Jinan 250358, China

[*]Corresponding author. Email: ylzheng@sjtu.edu.cn; xfchen@sjtu.edu.cn

[†]These authors contribute equally to this work.

1. Electric field analysis of sub-diffraction suspended dielectric cavities

The suspended circular Bragg gratings are engineered with a tailored radial period to support resonant operation across the 1250–1500 nm wavelength range. Starting from nonlinear Maxwell's equations and assuming a time-harmonic electric field of the form $\mathbf{E}(\mathbf{r},t) = \mathbf{E}(\mathbf{r})e^{-i\omega t}$.

In the absence of electrostatic interactions—that is, neglecting the free charge density ($\rho_f = 0$) and the free current density ($\mathbf{J}_f = 0$)—the nonlinear Maxwell's equations can be simplified under the high-frequency approximation (e.g., in the optical regime) as follows:

$$\begin{aligned} \nabla \cdot \mathbf{D} &= 0 \\ \nabla \cdot \mathbf{B} &= 0 \\ \nabla \times \mathbf{E} &= -\frac{\partial \mathbf{B}}{\partial t} \\ \nabla \times \mathbf{H} &= \frac{\partial \mathbf{D}}{\partial t} \end{aligned} \tag{S1}$$

In Eqn. S1, $\mathbf{D}$ and $\mathbf{H}$ are electric displacement field and magnetic fields of the eigenmodes, respectively, and t represents time. The solution form of Maxwell's equations in cylindrical coordinates is given in Eqn. S2.

$$\begin{gathered}\left[\frac{\partial^2}{\partial\rho^2}+\frac{1}{\rho}\frac{\partial}{\partial\rho}+\frac{1}{\rho^2}\frac{\partial^2}{\partial\varphi^2}\right]\mathbf{E}_j^{(\omega)}=-\mu_0\omega^2\mathbf{D}_j^{(\omega)} \\ \left(\frac{\partial\mathbf{D}_z}{\partial\rho}+\frac{1}{\rho}\frac{\partial\mathbf{D}_y}{\partial\varphi}\right)\cos\varphi+\left(\frac{\partial\mathbf{D}_y}{\partial\rho}-\frac{1}{\rho}\frac{\partial\mathbf{D}_z}{\partial\varphi}\right)\sin\varphi=0\end{gathered} \tag{S2}$$

Under the condition that only second-order nonlinear effects are considered, the components of the electric displacement field can be described as D_x, D_y, and D_z, satisfying Eqn. S3.

$$\begin{pmatrix}\mathbf{D}_x\\ \mathbf{D}_y\\ \mathbf{D}_z\end{pmatrix}=\varepsilon_0\begin{pmatrix}\varepsilon_{xx}&\varepsilon_{yx}&\varepsilon_{zx}\\ \varepsilon_{xy}&\varepsilon_{yy}&\varepsilon_{zy}\\ \varepsilon_{xz}&\varepsilon_{yz}&\varepsilon_{zz}\end{pmatrix}\begin{pmatrix}\mathbf{E}_x\\ \mathbf{E}_y\\ \mathbf{E}_z\end{pmatrix}+\varepsilon_0\begin{pmatrix}\sum_{j,k}\chi^{(2)}_{xjk}\mathbf{E}_j\mathbf{E}_k\\ \sum_{j,k}\chi^{(2)}_{yjk}\mathbf{E}_j\mathbf{E}_k\\ \sum_{j,k}\chi^{(2)}_{zjk}\mathbf{E}_j\mathbf{E}_k\end{pmatrix} \tag{S3}$$

Lithium niobate is a negative uniaxial crystal (point group $3m$). Its linear dielectric tensor in the crystal axis coordinate system is a diagonal matrix:

$$\boldsymbol{\varepsilon}=\begin{pmatrix}\varepsilon_{xx}&0&0\\ 0&\varepsilon_{yy}&0\\ 0&0&\varepsilon_{zz}\end{pmatrix} \tag{S4}$$

The last term in Eqn. S3 corresponds to the second-order nonlinear polarization, which can be expressed as

$$\mathbf{P}_i^{(2)}(2\omega)=\varepsilon_0\sum_{j,k}\chi^{(2)}_{ijk}\mathbf{E}_j(\omega)\mathbf{E}_k(\omega) \tag{S5}$$

where $\chi^{(2)}_{ijk}$ denotes the elements of the second-order nonlinear susceptibility tensor, and $\mathbf{E}_j(\omega)$, $\mathbf{E}_k(\omega)$ are the components of the fundamental electric field at frequency ω.

$$\begin{pmatrix}\mathbf{P}_x^{(2)}\\ \mathbf{P}_y^{(2)}\\ \mathbf{P}_z^{(2)}\end{pmatrix}=2\varepsilon_0\begin{pmatrix}d_{11}&d_{21}&d_{31}&d_{14}&d_{15}&d_{16}\\ d_{12}&d_{22}&d_{32}&d_{24}&d_{25}&d_{26}\\ d_{13}&d_{23}&d_{33}&d_{34}&d_{35}&d_{36}\end{pmatrix}\begin{pmatrix}\mathbf{E}_x(\omega)\mathbf{E}_x(\omega)\\ \mathbf{E}_y(\omega)\mathbf{E}_y(\omega)\\ \mathbf{E}_z(\omega)\mathbf{E}_z(\omega)\\ 2\mathbf{E}_y(\omega)\mathbf{E}_z(\omega)\\ 2\mathbf{E}_x(\omega)\mathbf{E}_z(\omega)\\ 2\mathbf{E}_x(\omega)\mathbf{E}_y(\omega)\end{pmatrix} \tag{S6}$$

For lithium niobate (point group $3m$), the nonzero d components are:

$$d_{31} = d_{32} \neq 0, \quad d_{33} \neq 0, \quad d_{15} = d_{24} \neq 0 \tag{S7}$$

Therefore, the nonlinear polarization terms can be further simplified as:

$$\begin{aligned} \mathbf{P}_x^{(2)} &= 2d_{15}\mathbf{E}_y\mathbf{E}_z \\ \mathbf{P}_y^{(2)} &= 2d_{15}\mathbf{E}_x\mathbf{E}_z \\ \mathbf{P}_z^{(2)} &= d_{31}\left(\mathbf{E}_x^2 + \mathbf{E}_y^2\right) + d_{33}\mathbf{E}_z^2 \end{aligned} \tag{S8}$$

The substitution of Eqn. S8 into Eqn. S3 yields the nonlinear polarization component $[\mathbf{D}_x(\omega), \mathbf{D}_y(\omega), \mathbf{D}_z(\omega)]$ as:

$$\begin{pmatrix} \mathbf{D}_x(\omega) \\ \mathbf{D}_y(\omega) \\ \mathbf{D}_z(\omega) \end{pmatrix} = \varepsilon_0 \begin{pmatrix} \varepsilon_{xx}(\omega)\mathbf{E}_x(\omega) + 2d_{15}\mathbf{E}_y(\omega)\mathbf{E}_z(\omega) \\ \varepsilon_{yy}(\omega)\mathbf{E}_y(\omega) + 2d_{15}\mathbf{E}_x(\omega)\mathbf{E}_z(\omega) \\ \varepsilon_{zz}(\omega)\mathbf{E}_z(\omega) + d_{31}\left(\mathbf{E}_x^2(\omega) + \mathbf{E}_y^2(\omega)\right) + d_{33}\mathbf{E}_z^2(\omega) \end{pmatrix} \tag{S9}$$

The second-order nonlinear optical effects are considered as higher-order perturbations in the electromagnetic field analysis. Therefore, in this work, we assume the second-order nonlinear susceptibility tensor components d_{33}, d_{31}, and d_{15} to be zero.

$$\begin{pmatrix} \mathbf{D}_x(\omega) \\ \mathbf{D}_y(\omega) \\ \mathbf{D}_z(\omega) \end{pmatrix} = \varepsilon_0 \begin{pmatrix} \varepsilon_{xx}(\omega)\mathbf{E}_x(\omega) \\ \varepsilon_{yy}(\omega)\mathbf{E}_y(\omega) \\ \varepsilon_{zz}(\omega)\mathbf{E}_z(\omega) \end{pmatrix} \tag{S10}$$

Substituting Eqn. S10 into Eqn. S2 yields Eqn. S11.

$$\begin{cases} \left[\dfrac{\partial^2}{\partial\rho^2} + \dfrac{1}{\rho}\dfrac{\partial}{\partial\rho} + \dfrac{1}{\rho^2}\dfrac{\partial^2}{\partial\varphi^2}\right]\mathbf{E}_i^{(\omega)} = -\dfrac{\omega^2}{c^2}n_{ii}^2(\omega)\mathbf{E}_i^{(\omega)} \\ \left[\dfrac{\partial}{\partial\rho}\left(n_{zz}^2(\omega)\mathbf{E}_z(\omega)\right) + \dfrac{1}{\rho}\dfrac{\partial}{\partial\varphi}\left(n_{yy}^2(\omega)\mathbf{E}_y(\omega)\right)\right]\cos\varphi \\ \quad + \left[\dfrac{\partial}{\partial\rho}\left(n_{yy}^2(\omega)\mathbf{E}_y(\omega)\right) - \dfrac{1}{\rho}\dfrac{\partial}{\partial\varphi}\left(n_{zz}^2(\omega)\mathbf{E}_z(\omega)\right)\right]\sin\varphi = 0 \end{cases} \tag{S11}$$

In the Eqn. S11, the anisotropic permittivity components $\varepsilon_{yy}(\omega)$ and $\varepsilon_{zz}(\omega)$ appear explicitly. These can be equivalently expressed in terms of the refractive indices $n_{yy}(\omega)$ and $n_{zz}(\omega)$ via the relation in Eqn. S12.

$$\varepsilon_{ii}(\omega) = n_{ii}^2(\omega), \quad i = x, y, z \tag{S12}$$

We assume that each component of the electric field can be expressed in a separable form as

$$E_i^{(\omega)}(\rho, \varphi) = R_i(\rho)\,\Phi_i(\varphi) \tag{S13}$$

where $R_i(\rho)$ and $\Phi_i(\varphi)$ represent the radial and angular components of the electric field, respectively. Due to the inherent periodicity of the angular coordinate φ (with period 2π), the angular function $\Phi_i(\varphi)$ is chosen as

$$\Phi_i(\varphi) = e^{im_i\varphi}, \quad m_i \in \mathbb{Z} \tag{S14}$$

where m_i is an integer ensuring the single-valuedness and periodicity of the wavefunction. Substituting the separated variables into the first equation yields

$$\frac{1}{R_i}\left(\frac{\mathrm{d}^2R_i}{\mathrm{d}\rho^2} + \frac{1}{\rho}\frac{\mathrm{d}R_i}{\mathrm{d}\rho}\right) - \frac{m_i^2}{\rho^2} = -\frac{\omega^2}{c^2}n_{ii}^2(\omega) \tag{S15}$$

By algebraic manipulation, we obtain the radial differential equation

$$\frac{\mathrm{d}^2R_i}{\mathrm{d}\rho^2} + \frac{1}{\rho}\frac{\mathrm{d}R_i}{\mathrm{d}\rho} + \left[k_i^2 - \frac{m_i^2}{\rho^2}\right]R_i = 0 \tag{S16}$$

where

$$k_i = \frac{\omega}{c}n_{ii}(\omega) \tag{S17}$$

Eqn. S16 is the standard Bessel equation, whose general solution can be expressed as a linear combination of Bessel functions:

$$R_i(\rho) = A_iJ_{m_i}(k_i\rho) + B_iY_{m_i}(k_i\rho) \tag{S18}$$

where $J_{m_i}(k_i\rho)$ is the first kind Bessel function, and $Y_{m_i}(k_i\rho)$ is the second kind Bessel function (also known as the Neumann function). The constants A_i and B_i are determined by boundary conditions.

Regular case without singularities. In typical cylindrical geometries where the domain includes the origin ($\rho = 0$) and no geometric singularity is present, the solution to the radial equation must be finite at $\rho = 0$. Since the second kind Bessel function, $Y_{m_i}(k_i\rho)$, diverges at the origin, the

physical requirement of regularity demands that its contribution be excluded. Thus, the general solution simplifies to:

$$R_i(\rho) = A_i J_{m_i}(k_i \rho) \tag{S19}$$

where A_i is a constant determined by boundary conditions.In this case, the electric field remains finite.

Case with bowtie-shaped singularities. In contrast, when a bowtie-shaped singularity—such as a sharp metallic tip or a subwavelength dielectric gap—is present near or at $\rho = 0$, the center is no longer a regular point in the domain. Such geometric features introduce a physical or mathematical singularity that invalidates the regularity condition at the origin.

In this scenario, the solution to the radial equation must retain both Bessel functions:

$$R_i(\rho) = A_i J_{m_i}(k_i \rho) + B_i Y_{m_i}(k_i \rho) \tag{S20}$$

where B_i takes nonzero values depending on the field behavior near the singularity. The divergent nature of Y_{m_i} at the origin is no longer unphysical, but may reflect genuine field enhancement arising from the singular structure. Such effects are particularly significant in dielectric nanogaps or nonlinear optical hotspots, where geometric singularities lead to localized field amplification. The higher-order small terms of the electric field can be neglected, and the eigenmodes **E** and **H** can be expressed in Eqn. S21.

$$
\begin{cases}
\mathbf{E}_y = \begin{cases}
\frac{\alpha}{\varepsilon_{yy}} C(k_0\rho)^{-l}\cos[l\varphi], & -\frac{\theta}{2} \le \varphi \le \frac{\theta}{2} \\
\frac{\alpha}{\varepsilon_{yy}} C(k_0\rho)^{-l}\cos\left[l(\pi-\varphi)\right], & \pi - \frac{\theta}{2} \le \varphi \le \pi + \frac{\theta}{2} \\
C(k_0\rho)^{-l}\cos\left[l\left(\frac{\pi}{2}+\varphi\right)\right], & -\pi + \frac{\theta}{2} < \varphi < -\frac{\theta}{2} \\
C(k_0\rho)^{-l}\cos\left[l\left(\frac{\pi}{2}-\varphi\right)\right], & \frac{\theta}{2} < \varphi < \pi - \frac{\theta}{2}
\end{cases} \\
\mathbf{E}_z = \begin{cases}
\frac{\alpha}{\varepsilon_{zz}} C(k_0\rho)^{-l}\sin[l\varphi], & -\frac{\theta}{2} \le \varphi \le \frac{\theta}{2} \\
-\frac{\alpha}{\varepsilon_{zz}} C(k_0\rho)^{-l}\sin\left[l(\pi-\varphi)\right], & \pi - \frac{\theta}{2} \le \varphi \le \pi + \frac{\theta}{2} \\
C(k_0\rho)^{-l}\sin\left[l\left(\frac{\pi}{2}+\varphi\right)\right], & -\pi + \frac{\theta}{2} < \varphi < -\frac{\theta}{2} \\
-C(k_0\rho)^{-l}\sin\left[l\left(\frac{\pi}{2}-\varphi\right)\right], & \frac{\theta}{2} < \varphi < \pi - \frac{\theta}{2}
\end{cases} \\
\mathbf{E}_x = 0 \\
\mathbf{H}_x = \mathbf{H}_y = \mathbf{H}_z = 0
\end{cases}
\tag{S21}
$$

The analytical solution suggests an infinite electric field intensity at the hotspot. Nevertheless, due to the impossibility of a zero gap distance in real structures, the field enhancement factor is ultimately finite.

2. Nonlinear coupling wave equation and SHG enhancement

In the absence of losses and under the slowly varying envelope approximation, the nonlinear coupled wave equations in the time-domain electromagnetic field can be expressed as shown in Eqn. S22.

$$
\begin{cases}
\dfrac{\mathrm{d}\tilde{\alpha}_1}{\mathrm{d}t} = -i\beta_1 \tilde{\alpha}_1^{*} \tilde{\alpha}_2 e^{-i(\omega_2 - 2\omega_1)t} \\
\dfrac{\mathrm{d}\tilde{\alpha}_2}{\mathrm{d}t} = i\beta_2 \tilde{\alpha}_1^{2} e^{-i(2\omega_1 - \omega_2)t}
\end{cases}
\tag{S22}
$$

In Eqn. (S22), $\tilde{\alpha}_1$ and $\tilde{\alpha}_2$ denote the complex slowly varying amplitudes of the coupled waves at frequencies ω_1 and ω_2, respectively, g represents the nonlinear coupling coefficient, ω_1 and ω_2 are the angular frequencies of the modes, the asterisk * denotes the complex conjugate.

Taking into account losses and input excitation, the nonlinear coupled wave equations are given in Eqn. S23.

$$\begin{cases} \dfrac{\mathrm{d}\tilde{\alpha}_1}{\mathrm{d}t} = -\dfrac{\kappa_{10}+\kappa_{1e}}{2}\tilde{\alpha}_1 + \sqrt{\kappa_{1e}}s\, e^{-i(\omega_p-\omega_1)t} - i\beta_1\, \tilde{\alpha}_1^*\tilde{\alpha}_2\, e^{-i(\omega_2-2\omega_1)t} \\ \dfrac{\mathrm{d}\tilde{\alpha}_2}{\mathrm{d}t} = -\dfrac{\kappa_{20}+\kappa_{2e}}{2}\tilde{\alpha}_2 + i\beta_2\, \tilde{\alpha}_1^2\, e^{-i(2\omega_1-\omega_2)t} \end{cases} \tag{S23}$$

where ω_p and s denote the frequency and the amplitude of the input electric field in the pump fibre, with $|s|^2$ being the input power, κ_{j0} and κ_{je} represent the intrinsic decay rate and external coupling rate, respectively. Under the assumption of solely second-order nonlinear effects, the nonlinear coupling coefficients β_1 and β_2 are defined as presented in Eqn. S24[45].

$$\begin{cases} \beta_1 = \dfrac{1}{4}\dfrac{\int \mathrm{d}^3x \sum_{ijk} \varepsilon\chi^{(2)}_{ijk}\left(\mathbf{E}^*_{1i}\mathbf{E}_{2j}\mathbf{E}^*_{1k} + \mathbf{E}^*_{1j}\mathbf{E}_{2k}\mathbf{E}^*_{1i}\right)}{\left(\int \mathrm{d}^3x\, \varepsilon|\mathbf{E}_1|^2\right)\left(\int \mathrm{d}^3x\, \varepsilon|\mathbf{E}_2|^2\right)^{1/2}} \\ \beta_2 = \dfrac{1}{4}\dfrac{\int \mathrm{d}^3x \sum_{ijk} \varepsilon\chi^{(2)}_{ijk}\mathbf{E}^*_{2i}\mathbf{E}_{1j}\mathbf{E}_{1k}}{\left(\int \mathrm{d}^3x\, \varepsilon|\mathbf{E}_1|^2\right)\left(\int \mathrm{d}^3x\, \varepsilon|\mathbf{E}_2|^2\right)^{1/2}} \end{cases} \tag{S24}$$

In the rotating frame of the pump, $\alpha_1 = \tilde{\alpha}_1 e^{i(\omega_p-\omega_1)t}$ and $\alpha_2 = \tilde{\alpha}_2 e^{i(2\omega_p-\omega_2)t}$, the coupled wave equations can be expressed in Eqn. S25.

$$\begin{cases} \dfrac{\mathrm{d}\alpha_1}{\mathrm{d}t} = \left[i(\omega_p-\omega_1) - \dfrac{\kappa_{10}+\kappa_{1e}}{2}\right]\alpha_1 + \sqrt{\kappa_{1e}}s - i\beta_1\alpha_1^*\alpha_2 \\ \dfrac{\mathrm{d}\alpha_2}{\mathrm{d}t} = \left[i(2\omega_p-\omega_2) - \dfrac{\kappa_{20}+\kappa_{2e}}{2}\right]\alpha_2 + i\beta_2\alpha_1^2 \end{cases} \tag{S25}$$

The pump is almost unperturbed by SHG, since the pump light is much stronger than the SH signal. Therefore, the last term in Eqn. S25 can be ignored in the following analysis. Considering the steady state, i.e., $\frac{\mathrm{d}\tilde{\alpha}_1}{\mathrm{d}t} = \frac{\mathrm{d}\tilde{\alpha}_2}{\mathrm{d}t} = 0$, the above coupled mode equations result in the expression of generated SH power[46],

$$P_2 = \frac{4|\boldsymbol{\beta}|^2 Q_2^2}{\omega_2 Q_{2e}\left[4Q_2^2\left(\frac{2\omega_p}{\omega_2}-1\right)^2+1\right]} \cdot \frac{16Q_1^4}{Q_{1e}^2\,\omega_1^2\left[4Q_1^2\left(\frac{\omega_p}{\omega_1}-1\right)^2+1\right]^2}P_1^2 \tag{S26}$$

Here, $Q_j = \frac{\omega_j}{\kappa_{j0}+\kappa_{je}}$ and $Q_{je} = \frac{\omega_j}{\kappa_{je}}$ denote the loaded quality factor and the external (coupling-induced) quality factor, respectively. Under the phase-matching condition, i.e., $\omega_p = \omega_1 = \omega_2/2$, and assuming critical coupling ($Q_j = Q_{je}$), the conversion efficiency scales as $\frac{P_2}{P_1^2} \propto Q_2 Q_1^2|\beta|^2$.

From Eqn. S24, we can derive the relationship between the mode volume V_{m} and the coupling coefficients. In this case, any integral over the fields will simply yield the mode volume V_{m} of the nonlinear material. Thus, for the $\chi^{(2)}$ effect, we obtain $\beta_i \sim g\frac{\chi^{(2)}}{\sqrt{V_{\mathrm{m}}}}$, where g represents the coupling coefficient into the cavity. In fact, although the calculated mode volume is very small, the overall enhancement factor does not increase significantly because the coupling coefficient between the Gaussian beam and the nanocavity is quite small, resulting in a relatively small value of g.

3. Fabrication of suspended CBGs and bowtie structures in suspended CBG

The fabrication process of the suspended CBG structure with an integrated bowtie consists of several steps, as illustrated in Fig. S1. Firstly, a 600-nm-thick amorphous silicon is deposited on the TFLN wafer via plasma-enhanced chemical vapor deposition (PECVD), followed by spin-coating of ZEP520A electron beam resist. The designed patterns are then exposed by electron beam lithography and developed by pentyl acetate. Subsequently, the pattern is transferred to the silicon layer using inductively coupled plasma reactive ion etching (ICP-RIE). The underlying TFLN is further etched via ICP to form the nanostructures. Afterward, the silicon hard mask is removed, and selective wet etching of the buried SiO_2 layer is performed to release the suspended structure.

4. Experimental setup for reflection measurement

As shown in Fig. S2, the light source is a picosecond supercontinuum laser with a pulse duration of 220 ps (YSL photonics SC-pro, repetition rate: 20 MHz). The supercontinuum is firstly filtered by a long-pass filter (>1250 nm). The input light is then tightly focused on the sample by a NIR microscope objective (Mitutoyo 50×, NA = 0.65). Reflection light is collected by the same objective and reflected by a beam splitter (50:50, 600–1700 nm). A flip mirror is added after the beam splitter to guide the beam into two arms. The light is either coupled into a multimode fiber and recorded by a spectrometer (Anritsu, MS9740A) or imaged using a camera (EMCCD, iXon Ultra 897).

5. Experimental setup for SHG enhancement

As shown in Fig. S3, during the SHG signal measurement, the supercontinuum source is spectrally filtered using a tunable high-power filter (YSL Photonics AOTF-PRO2, FWHM 1.9 nm). The

output beam then passes through a Glan prism and half-wave plate (@1310 nm) to adjust the polarization of the excitation light. Afterward, the beam is directed through two beam splitters (BS) and a microscope objective, tightly focused onto the center of the sample. The reflected signal is redirected by the same plate beam splitter to a EMCCD camera (iXon Ultra 897) for measuring the SHG intensity of the sample, or alternatively, coupled into a spectrometer (Ocean Optics, HR4000) via a fiber coupling system to analyze the SHG spectrum.

6. Design of suspended CBGs and bowtie structures in suspended CBG

The sample is simulated using the finite-difference time-domain (FDTD) method. To enhance the refractive index contrast, suspended supports are designed within the circular Bragg cavity, as shown in Fig. S4. The size of the supporting structures is minimized—down to 90 nm—to ensure sufficient mechanical stability while preventing the collapse of the sample.

By tuning the period and duty cycle of the sample, different resonant structures can be engineered. Using the FDTD method, structures with periods ranging from 720 to 840 nm and duty cycles between 0.58 and 0.66 are designed. The resonance wavelength can be shifted by adjusting the period (Fig. S5-S8). Considering that the etching angle depends on both the grating period and duty cycle, the designed resonances are centered at around 1310 nm.

7. Discussion of electric field distributions of bowtie with different gap sizes

The electric field distribution within the bowtie structure is strongly influenced by the gap size. As the gap narrows, the electromagnetic coupling between the two dielectric tips intensifies, leading to a significant increase in the local field enhancement at the dielectric gap (Fig. S9). This enhanced confinement can greatly improve nonlinear optical effects like SHG.

However, reducing the gap size also presents fabrication challenges and may introduce additional losses or scattering due to imperfections. The field confinement becomes more spatially localized in smaller gaps, requiring high fabrication precision to fully utilize the enhancement. In our work, the fabrication limit of the gap size is 20 nm (Fig. S10).

8. Discussion of related work

Bowtie nanostructure integrated within a suspended circular Bragg cavity has been experimentally and theoretically designed, enabling giant SHG enhancement beyond the diffraction limit. The information of the fundamental and second harmonic signals is shown in Tables S1 and S2. The CBG nanocavity achieves a high normalized conversion efficiency of 0.85×10^{-2} cm^2/GW under a pump intensity of 1 MW/cm^2, with a mode volume as small as 7.58×10^{-4} $(\lambda/n)^3$. An SHG enhancement factor of 3,720 is achieved compared to bare TFLN. Efficient SHG under ultralow pump intensities is also demonstrated, significantly improving both the device performance and operational lifetime, while simultaneously reducing the mode volume.

In contrast to plasmonic resonances, the bowtie-integrated CBG structure is free from thermal losses and supports higher optical powers, significantly extending the upper limit of nonlinear conversion efficiency while maintaining an ultrasmall mode volume. Furthermore, compared to other all-dielectric nanostructures, our design exhibits a significantly reduced mode volume while maintaining a high SHG efficiency. The comparison is shown in Fig. 5H and Table S3. Notably, this work represents the first experimental realization of a nonlinear optical response beyond the diffraction limit in a all-dielectric nanocavity.

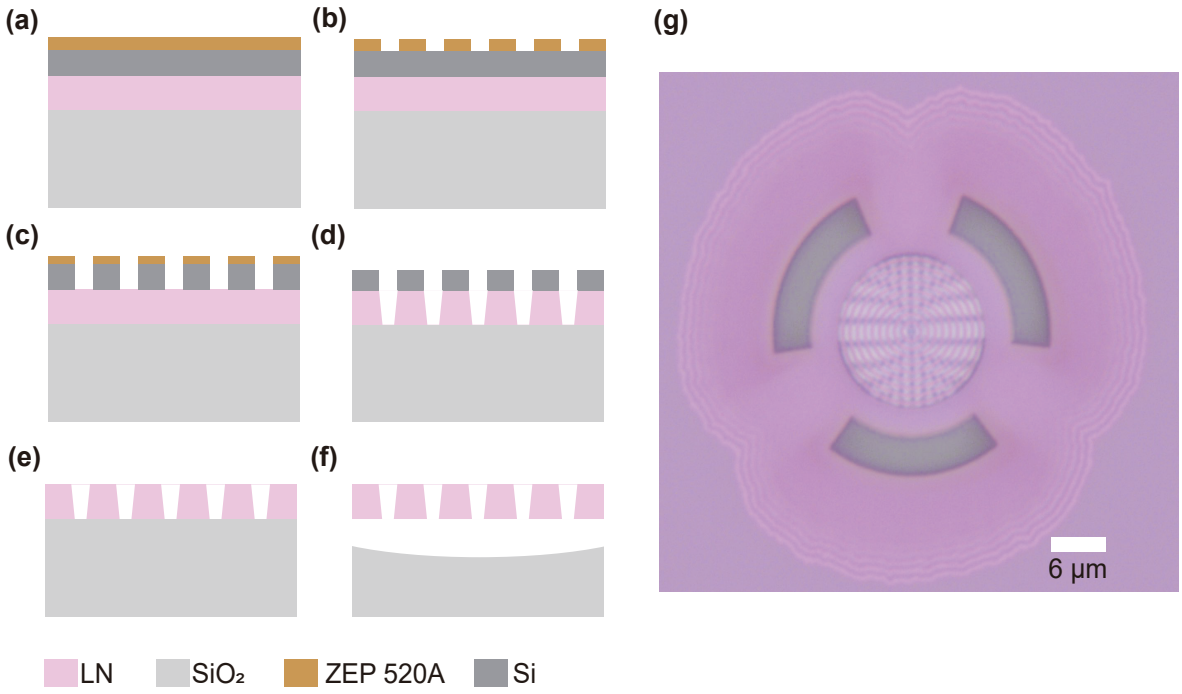

Figure S1: **Fabrication flowchart of the sample.** (**a**) Deposition of 600-nm amorphous silicon on TFLN via PECVD, followed by spin coating of ZEP520A photoresist. (**b**) Electron beam exposure and development. (**c**) ICP-RIE etching of silicon mask. (**d**) RIE etching of LN. (**e**) Removal of silicon. (**f**) Selective etching of silicon dioxide. (**g**) Optical microscope image of the sample.

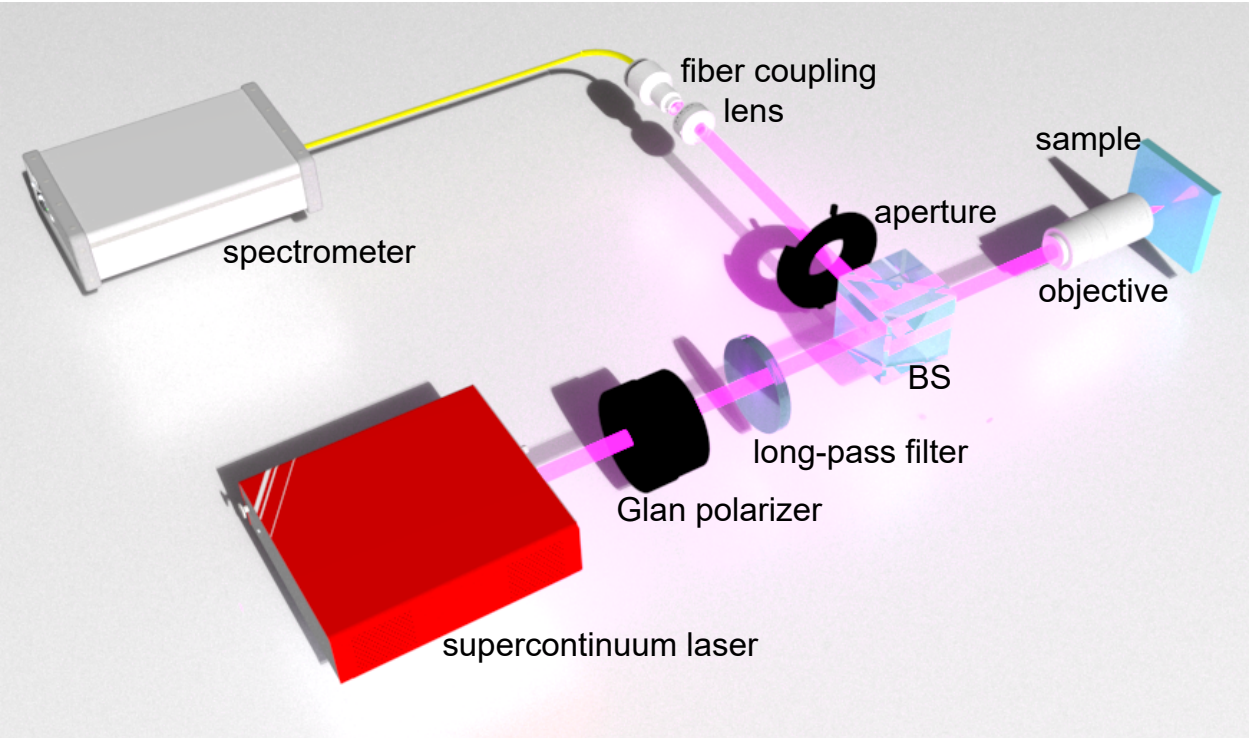

Figure S2: **Experimental setup for reflection measurement.** The supercontinuum laser (YSL photonics SC-pro, 430–2400 nm) passes a Glan polarizer for polarization control. Then, it is filtered by a long-pass filter (>1250 nm), to avoid the intense seed at 1064 nm. The input light is then tightly focused on the sample by a NIR microscope objective (Mitutoyo, 50×, NA=0.65). The reflection signal is collected by the same objective and reflected by a beam splitter (50:50, 600–1700 nm). The reflection signal is coupled into a single-mode optical fiber (the coupling efficiency is 30%) and recorded by a spectrometer (Anritsu, MS9740A).

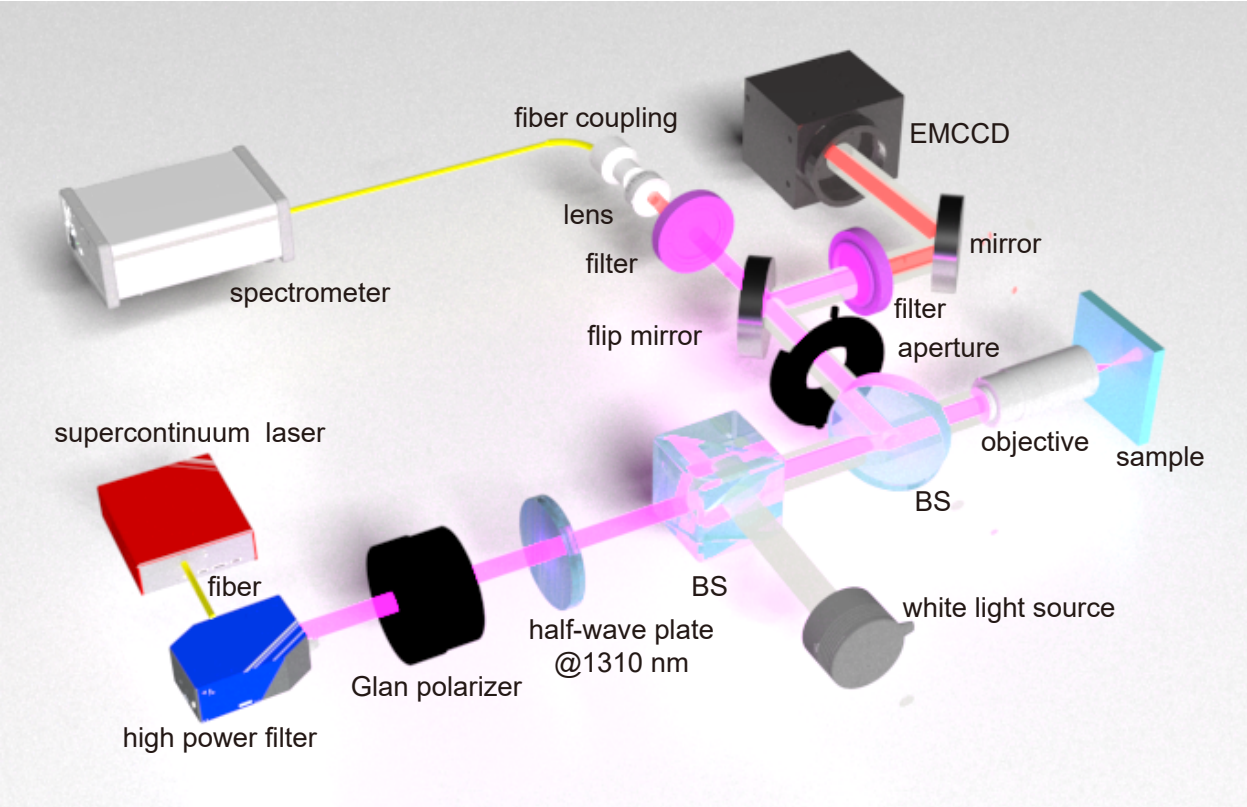

Figure S3: **Experimental setup for SHG enhancement.** During the SHG signal measurement, the supercontinuum source is spectrally filtered using a tunable high-power filter (YSL Photonics AOTF-PRO2, FWHM 1.9 nm). The output beam then passes through a Glan prism and half-wave plate (@1310 nm) to adjust the polarization of the excitation light. Afterward, the beam is directed through two beam splitters (BS) and a microscope objective, tightly focused onto the center of the sample. The reflected signal is redirected by the same plate beam splitter to a EMCCD camera (iXon Ultra 897) for measuring the SHG intensity of the sample, or alternatively, coupled into a spectrometer (Ocean Optics, HR4000) via a fiber coupling system to analyze the SHG spectrum.

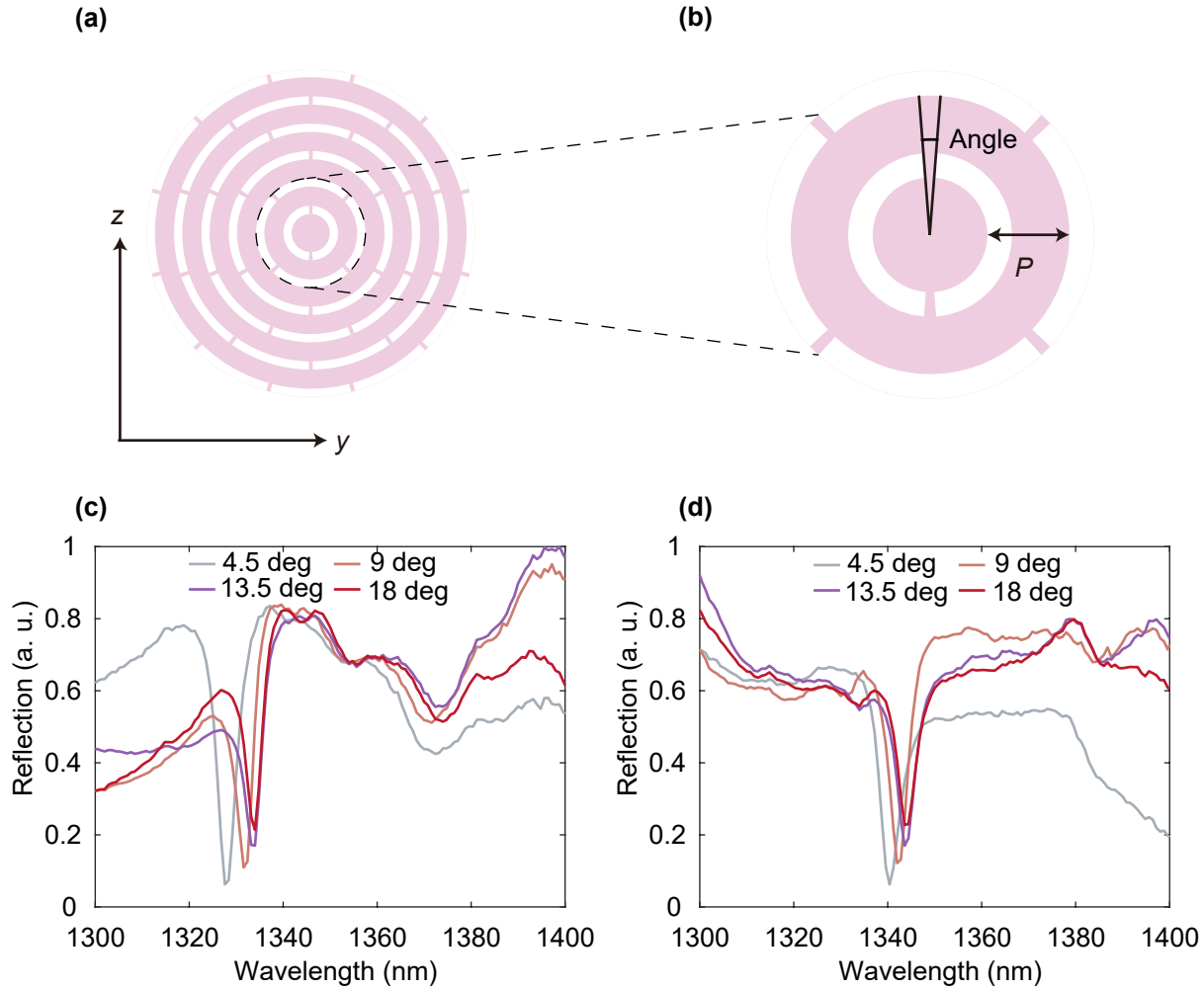

Figure S4: **Influence of the width of the suspended supports on the resonance.** (**a** and **b**) Schematics of the suspended supports in the CBG, illustrating that smaller angles correspond to reduced support size. (**c** and **d**) Reflection spectra under z-polarized and y-polarized pump excitation. A decrease in angle leads to an increased Q factor.

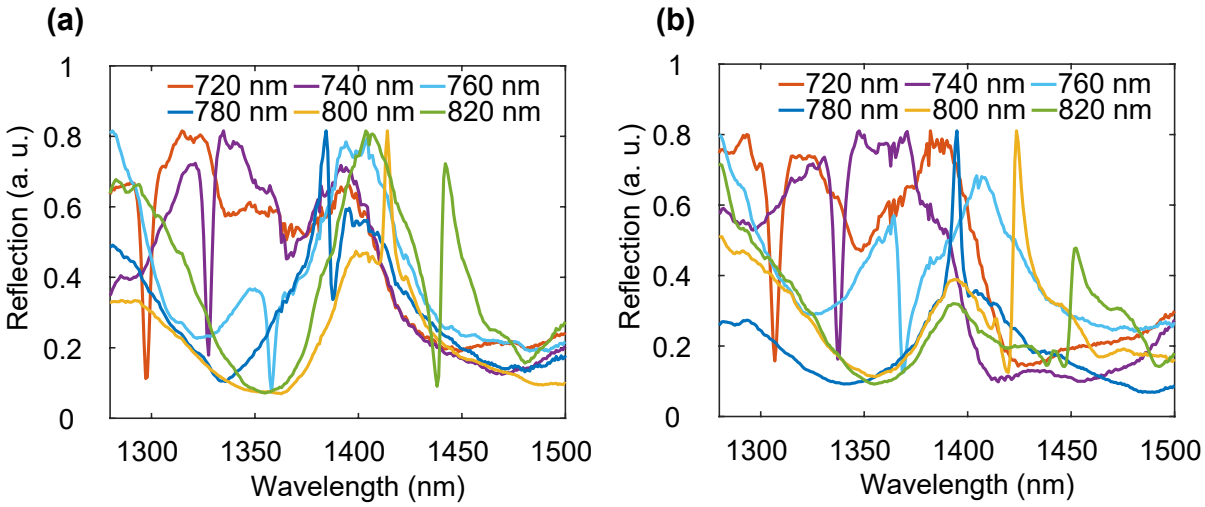

Figure S5: Experimental reflection spectra of suspended CBGs with different *P* values under (**a**) z-polarized and (**b**) y-polarized illumination.

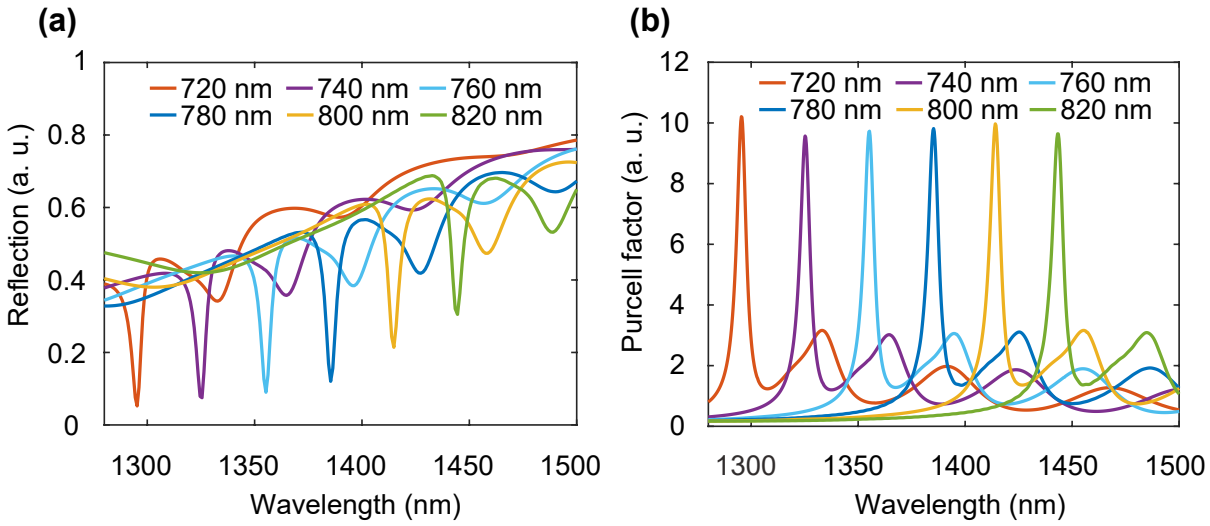

Figure S6: (**a**) Simulated reflection spectra of the suspended CBG under z-polarized illumination and (**b**) the corresponding Purcell factors.

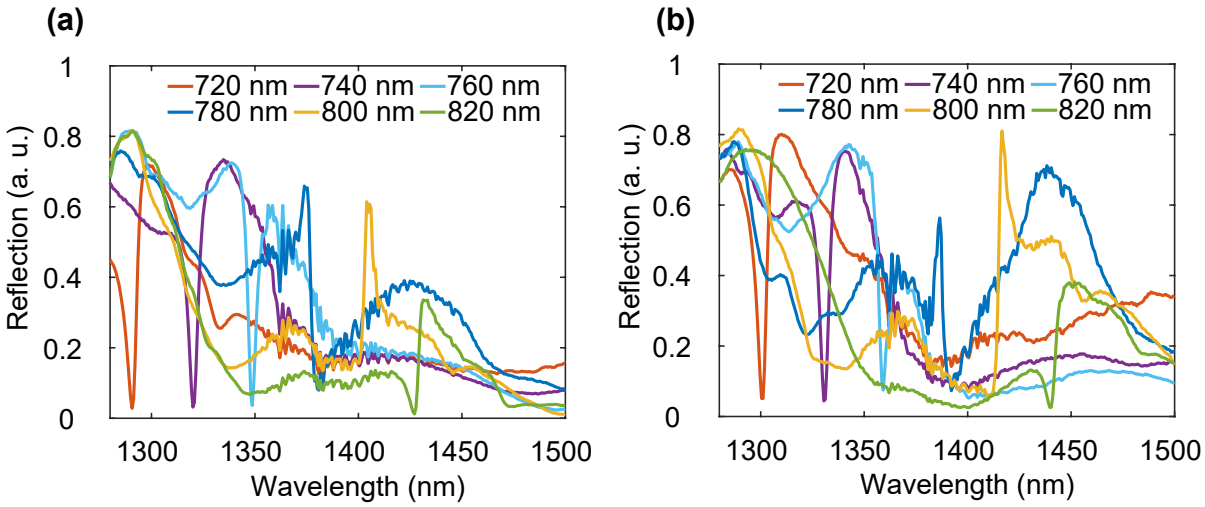

Figure S7: Experimental reflection spectra of bowtie in suspended CBG with different *P*'s under (**a**) z-polarized and (**b**) y-polarized illumination.

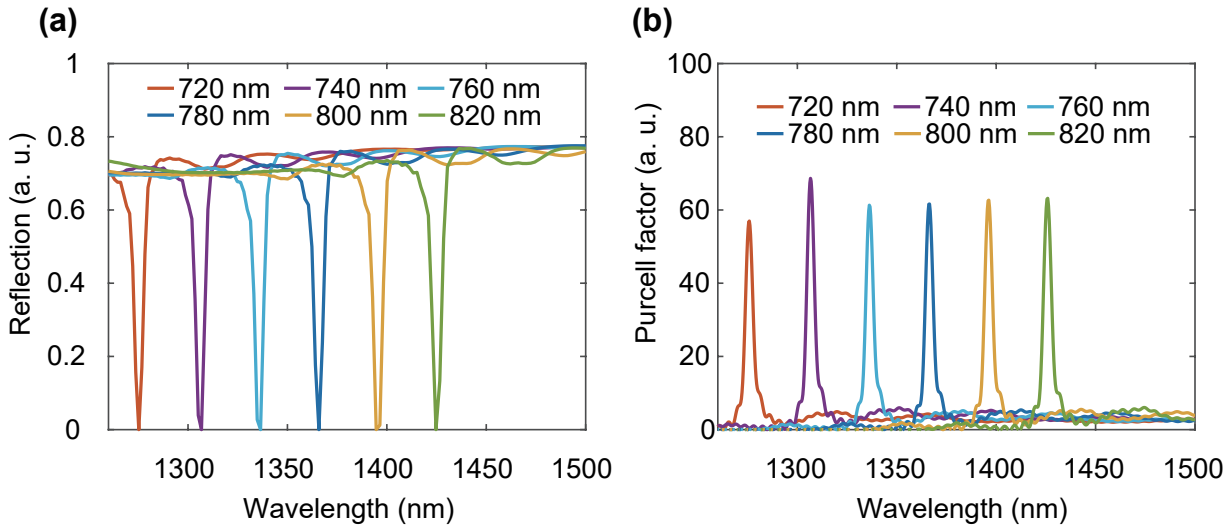

Figure S8: (**a**) Simulated reflection spectra of the bowtie in suspended CBG under z-polarized illumination and (**b**) the corresponding Purcell factors.

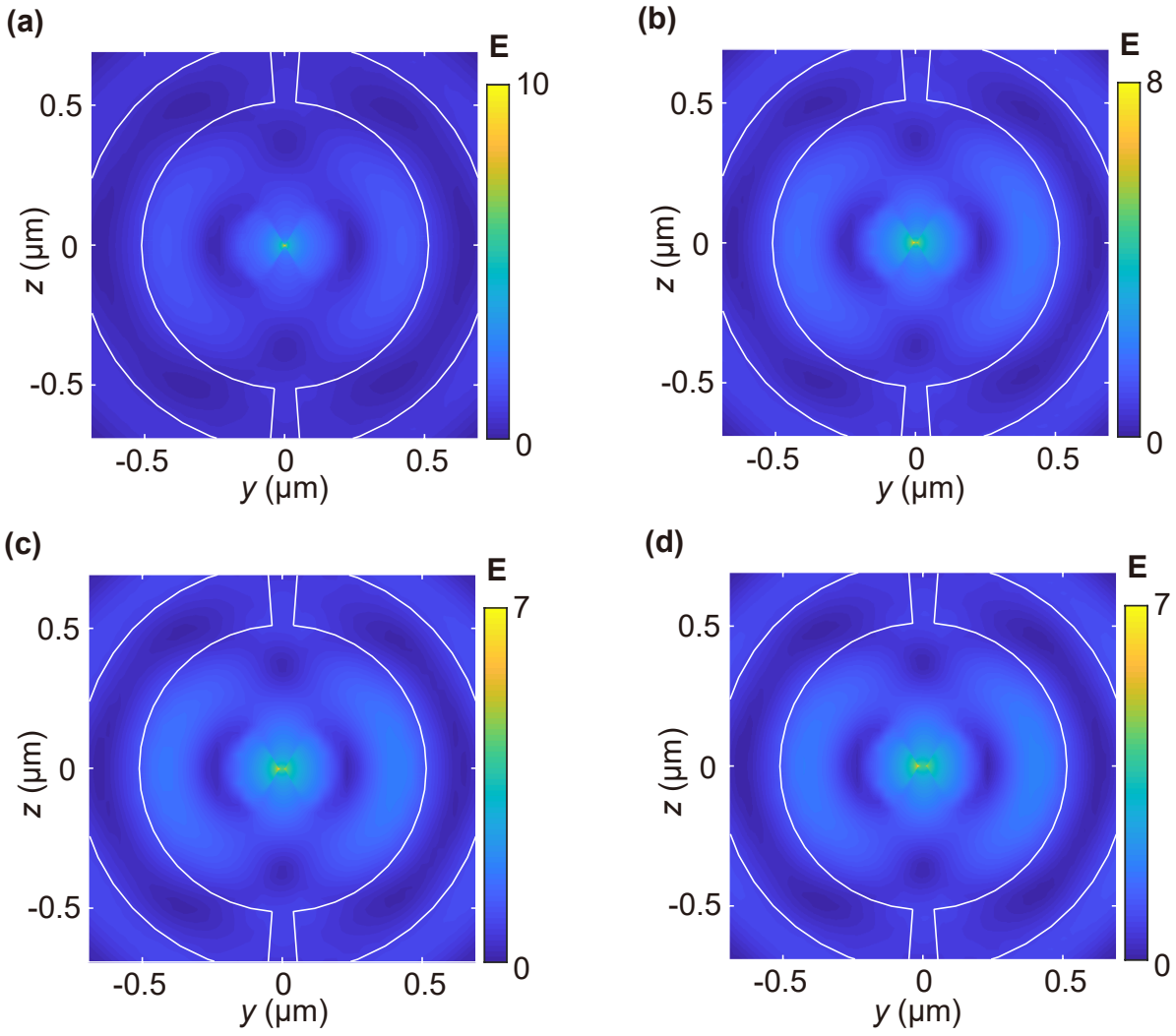

Figure S9: Simulated electric field distributions of the bowtie in suspended CBG structures with gap sizes of (**a**) 0 nm, (**b**) 10 nm, (**c**) 20 nm, and (**d**) 30 nm.

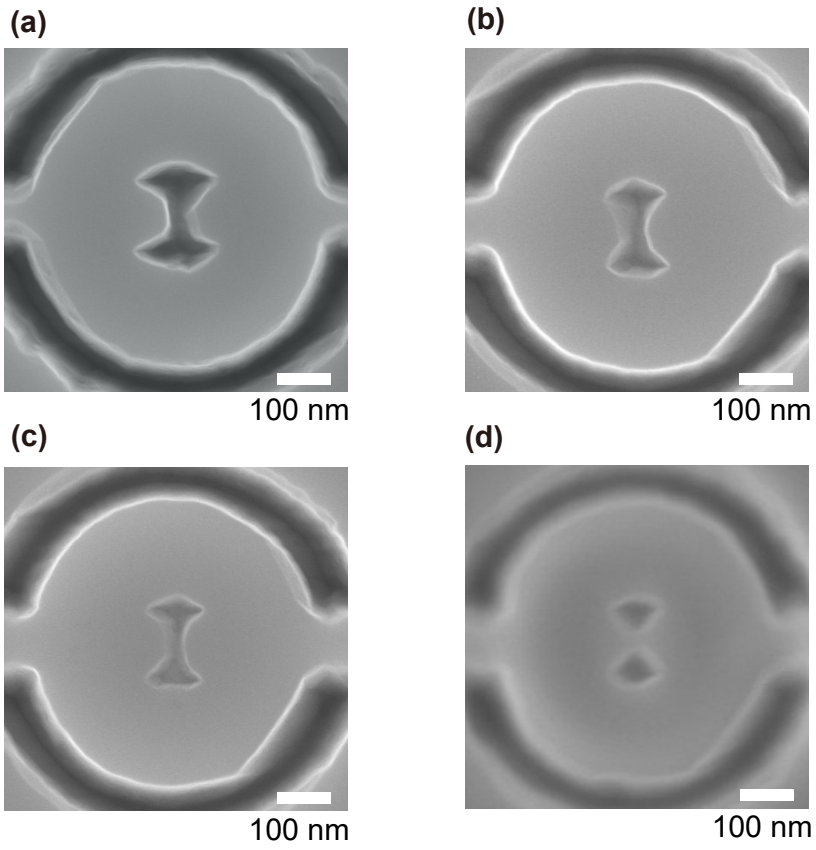

Figure S10: The fabricated sample is designed with a minimum gap of 20 nm. Due to the inclined etching angle, the actual separation at the tip of the sloped sidewalls is effectively reduced to 0 nm.

Table S1: **Experimental parameters and input power levels.** The table lists the laser excitation parameters, including wavelength, repetition rate, and pulse width, as well as the calculated spot diameter and peak power.

Parameter	Wavelength (nm)	Rep. rate (MHz)	Pulse length (ps)	Avg. power (mW)	NA –	Spot diameter (μm)	Peak power (mW)
Symbol	λ	ν	τ	P_{FH}	–	δ	$\hat{P}_{\mathrm{FH}}$
Formula	N/A	N/A	N/A	N/A	N/A	$\frac{1.22\lambda}{\mathrm{NA}}$	$\frac{P_{\mathrm{FH}}}{\nu\tau}$
Value	1310	20	220	0.21	0.65	2.46	47.7

Table S2: **SHG conversion efficiency** The table lists SHG related parameters in our experiment including SHG power, peak power, conversion efficiency, peak SHG efficiency, and normalized efficiency.

Parameter	SHG Power (nW)	SHG Peak Power (W)	Max. conv. eff. –	Peak SHG eff. (W^{-1})	Normalized SHG eff. (cm^2/GW)
Symbol	P_{SH}	$\hat{P}_{\mathrm{SH}}$	η_{SHG}	γ_{SHG}	η_{norm}
Formula	$N \cdot E_{\mathrm{ph}}$	$\frac{\hat{P}_{\mathrm{SH}}}{\nu\tau}$	$\frac{P_{\mathrm{SH}}}{P_{\mathrm{FH}}}$	$\frac{\hat{P}_{\mathrm{SH}}}{\hat{P}_{\mathrm{FH}}^2}$	$\frac{\eta_{\mathrm{SHG}} \cdot \pi \left(\frac{\delta}{2}\right)^2}{\hat{P}_{\mathrm{FH}}}$
Value	1.8	4.09×10^{-7}	8.6×10^{-6}	1.78×10^{-4}	0.85×10^{-2}

Table S3: **Comparison of nonlinear optical performance across nanophotonic platforms.** This table compares the Q factor, mode volume, SHG efficiency, and normalized SHG efficiency of various reported nanophotonic resonators.

Type	Q factor	Mode volume	Wavelength	SHG efficiency	Norm. SHG efficiency	Reference
	–	$(\lambda/n)^3$	(nm)	–	(cm^2/GW)	
This work	~370	7.58×10^{-4}	1310	8.6×10^{-6}	0.85×10^{-2}	N/A
Plasmonic	~20	6.45×10^{-6}	1550	6.4×10^{-9}	7.88×10^{-9}	Nat. Nanotechnol. **10**, 412 (2015)[10]
Plasmonic	~10	1.63×10^{-7}	850	0.87×10^{-6}	9.92×10^{-8}	Nat. Commun. **12**, 4326 (2021)[14]
Plasmonic	~30	6×10^{-6}	1560	1.3×10^{-7}	1.23×10^{-7}	Opt. Express **32**, 13140 (2024)[15]
Plasmonic	~10	1.3×10^{-7}	1560	N/A	N/A	Nano Lett. **15**, 4102 (2015)[11]
Plasmonic	~5	5×10^{-2}	650	3.7×10^{-12}	2.8×10^{-13}	Light Sci. Appl. **7**, 49 (2018)[16]
Plasmonic	N/A	5×10^{-4}	800–1300	1.13×10^{-6}	1.29×10^{-7}	Nat. Commun. **12**, 6425 (2021)[17]
Plasmonic	~10	1.4×10^{-7}	725–800	2×10^{-9}	1.8×10^{-8}	ACS Photonics **10**, 1529 (2023)[18]
BIC	~4000	0.5–2	1200	4×10^{-5}	4×10^{-3}	Nano Lett. **20**, 8745 (2020)[23]
BIC	~188	~0.07	1570	1.18×10^{-5}	1.6×10^{-4}	Science **367**, 288 (2020)[24]
PhC	~100	~100	742	2.8×10^{-3}	6.7×10^{-4}	Adv. Funct. Mater. **33**, 2308484 (2023)[19]
PhC	~100	~100	843	1×10^{-3}	4.7×10^{-4}	Adv. Opt. Mater. **13**, 2402686 (2023)[20]
PhC	8000	~1.18	1510	5.21×10^{-9}	N/A	Nanophotonics **13**, 4029 (2024)[21]
PhC	5600	~0.3	1500	3×10^{-11}	4.4×10^{-9}	Nano Lett. **24**, 11327 (2024)[22]
Anapole	~10	~7	1440	1.18×10^{-8}	6.1×10^{-10}	Adv. Mater. **37**, 2418257 (2024)[31]
Anapole	~5	~1.17	~800	1.9×10^{-5}	1.9×10^{-5}	Nano Lett. **18**, 3695 (2018)[29]
Mie	~20	~0.15	1400	3.4×10^{-10}	1.87×10^{-12}	Nat. Commun. **12**, 5597 (2021)[25]
Mie	~10	~1.58	900	5×10^{-8}	3.77×10^{-9}	Laser Photonics Rev. **16**, 2100604 (2022)[26]
Mie	~10	~10	820	2×10^{-6}	9.75×10^{-7}	Laser Photonics Rev. **15**, 2000521 (2021)[27]
Metasurface	~75	~1.38	940	2×10^{-4}	8.3×10^{-5}	Nano Lett. **22**, 9652 (2022)[40]
GMR	~4000	~110	1550	3×10^{-8}	2.03×10^{-5}	Phys. Rev. Lett. **127**, 153901 (2021)[28]
CBG/EBG	~260	~1.12	1310	2.32×10^{-5}	1.21×10^{-2}	Nano Lett. **24**, 11676 (2024)[42]

References

1. Y. Wang, *et al.*, Stable, high-performance sodium-based plasmonic devices in the near infrared. *Nature* **581** (7809), 401–405 (2020).

2. Y.-H. Ouyang, H.-Y. Luan, Z.-W. Zhao, W.-Z. Mao, R.-M. Ma, Singular dielectric nanolaser with atomic-scale field localization. *Nature* **632** (8024), 287–293 (2024).

3. W. Liu, *et al.*, Single-molecule sensing inside stereo-and regio-defined hetero-nanopores. *Nature Nanotechnology* pp. 1–9 (2024).

4. E. Deist, J. A. Gerber, Y.-H. Lu, J. Zeiher, D. M. Stamper-Kurn, Superresolution microscopy of optical fields using tweezer-trapped single atoms. *Physical Review Letters* **128** (8), 083201 (2022).

5. M. Kauranen, A. V. Zayats, Nonlinear plasmonics. *Nature Photonics* **6** (11), 737–748 (2012).

6. G. Li, S. Zhang, T. Zentgraf, Nonlinear photonic metasurfaces. *Nature Reviews Materials* **2** (5), 1–14 (2017).

7. T. Santiago-Cruz, *et al.*, Resonant metasurfaces for generating complex quantum states. *Science* **377** (6609), 991–995 (2022).

8. J. Zhang, *et al.*, Spatially entangled photon pairs from lithium niobate nonlocal metasurfaces. *Science Advances* **8** (30), eabq4240 (2022).

9. D. K. Gramotnev, S. I. Bozhevolnyi, Plasmonics beyond the diffraction limit. *Nature photonics* **4** (2), 83–91 (2010).

10. M. Celebrano, *et al.*, Mode matching in multiresonant plasmonic nanoantennas for enhanced second harmonic generation. *Nature Nanotechnology* **10** (5), 412–417 (2015).

11. M.-K. Kim, *et al.*, Squeezing photons into a point-like space. *Nano Letters* **15** (6), 4102–4107 (2015).

12. J. B. Khurgin, Ultimate limit of field confinement by surface plasmon polaritons. *Faraday Discussions* **178**, 109–122 (2015).

13. J. B. Khurgin, How to deal with the loss in plasmonics and metamaterials. *Nature Nanotechnology* **10** (1), 2–6 (2015).

14. G.-C. Li, *et al.*, Light-induced symmetry breaking for enhancing second-harmonic generation from an ultrathin plasmonic nanocavity. *Nature Communications* **12** (1), 4326 (2021).

15. Z. Li, *et al.*, Plasmonic hotspot arrays boost second harmonic generation in thin-film lithium niobate. *Optics Express* **32** (8), 13140–13155 (2024).

16. M. Galanty, *et al.*, Second harmonic generation hotspot on a centrosymmetric smooth silver surface. *Light: Science & Applications* **7** (1), 49 (2018).

17. J. Li, *et al.*, Full-color enhanced second harmonic generation using rainbow trapping in ultrathin hyperbolic metamaterials. *Nature Communications* **12** (1), 6425 (2021).

18. T. Zhang, Q. Guo, Z. Shi, S. Zhang, H. Xu, Coherent second harmonic generation enhanced by coherent plasmon–exciton coupling in plasmonic nanocavities. *ACS Photonics* **10** (5), 1529–1537 (2023).

19. L. Qu, *et al.*, Bright second harmonic emission from photonic crystal vertical cavity. *Advanced Functional Materials* **33** (47), 2308484 (2023).

20. L. Bai, *et al.*, Wavelength Tunable Second Harmonic Generation from Photonic Crystal Vertical Cavities. *Advanced Optical Materials* **13** (8), 2402686 (2025).

21. Z. Liu, *et al.*, Enhanced vertical second harmonic generation from layered GaSe coupled to photonic crystal circular Bragg resonators. *Nanophotonics* **13** (21), 4029–4035 (2024).

22. X. Wang, *et al.*, Experimental demonstration of high-efficiency harmonic generation in photonic moiré superlattice microcavities. *Nano Letters* **24** (36), 11327–11333 (2024).

23. A. P. Anthur, *et al.*, Continuous wave second harmonic generation enabled by quasi-bound-states in the continuum on gallium phosphide metasurfaces. *Nano Letters* **20** (12), 8745–8751 (2020).

24. K. Koshelev, *et al.*, Subwavelength dielectric resonators for nonlinear nanophotonics. *Science* **367** (6475), 288–292 (2020).

673 25. M. Nauman, *et al.*, Tunable unidirectional nonlinear emission from transition-metal-
674 dichalcogenide metasurfaces. *Nature Communications* **12** (1), 5597 (2021).

675 26. A. A. Popkova, *et al.*, Nonlinear exciton-mie coupling in transition metal dichalcogenide
676 nanoresonators. *Laser & Photonics Reviews* **16** (6), 2100604 (2022).

677 27. J. Ma, *et al.*, Nonlinear lithium niobate metasurfaces for second harmonic generation. *Laser &*
678 *Photonics Reviews* **15** (5), 2000521 (2021).

679 28. S. Yuan, *et al.*, Strongly enhanced second harmonic generation in a thin film lithium niobate
680 heterostructure cavity. *Physical Review Letters* **127** (15), 153901 (2021).

681 29. M. Timofeeva, *et al.*, Anapoles in free-standing III–V nanodisks enhancing second-harmonic
682 generation. *Nano Letters* **18** (6), 3695–3702 (2018).

683 30. G. Zograf, *et al.*, Combining ultrahigh index with exceptional nonlinearity in resonant transition
684 metal dichalcogenide nanodisks. *Nature Photonics* **18** (7), 751–757 (2024).

685 31. R. Biswas, *et al.*, Leveraging Strong Electric Field Gradients at Anapole Resonances for En-
686 hanced Second Harmonic Generation from Molybdenum Disulfide Disks. *Advanced Materials*
687 **37** (14), 2418257 (2025).

688 32. H. Shim, F. Monticone, O. D. Miller, Fundamental limits to the refractive index of transparent
689 optical materials. *Advanced Materials* **33** (43), 2103946 (2021).

690 33. J. B. Khurgin, Expanding the photonic palette: exploring high index materials. *ACS Photonics*
691 **9** (3), 743–751 (2022).

692 34. H. Choi, M. Heuck, D. Englund, Self-similar nanocavity design with ultrasmall mode volume
693 for single-photon nonlinearities. *Physical Review Letters* **118** (22), 223605 (2017).

694 35. S. Hu, *et al.*, Experimental realization of deep-subwavelength confinement in dielectric optical
695 resonators. *Science Advances* **4** (8), eaat2355 (2018).

696 36. M. Albrechtsen, *et al.*, Nanometer-scale photon confinement in topology-optimized dielectric
697 cavities. *Nature Communications* **13** (1), 6281 (2022).

37. A. N. Babar, *et al.*, Self-assembled photonic cavities with atomic-scale confinement. *Nature* **624** (7990), 57–63 (2023).

38. S. Gafsi, J. D. Ryckman, All-Dielectric Metawaveguide Ring Resonators with Deeply Sub-Diffractive Mode Volumes. *Laser & Photonics Reviews* p. 2401579 (2025).

39. C. Wang, *et al.*, Integrated lithium niobate electro-optic modulators operating at CMOS-compatible voltages. *Nature* **562** (7725), 101–104 (2018).

40. L. Qu, *et al.*, Giant second harmonic generation from membrane metasurfaces. *Nano Letters* **22** (23), 9652–9657 (2022).

41. A. Boes, *et al.*, Lithium niobate photonics: Unlocking the electromagnetic spectrum. *Science* **379** (6627), eabj4396 (2023).

42. Z. Li, *et al.*, Enhanced second-harmonic generation in thin-film lithium niobate circular Bragg nanocavity. *Nano Letters* **24** (37), 11676–11682 (2024).

43. H. Wang, *et al.*, Towards optimal single-photon sources from polarized microcavities. *Nature Photonics* **13** (11), 770–775 (2019).

44. O. Iff, *et al.*, Purcell-enhanced single photon source based on a deterministically placed WSe2 monolayer quantum dot in a circular Bragg grating cavity. *Nano Letters* **21** (11), 4715–4720 (2021).

45. A. Rodriguez, M. Soljačić, J. D. Joannopoulos, S. G. Johnson, χ (2) and χ (3) harmonic generation at a critical power in inhomogeneous doubly resonant cavities. *Optics Express* **15** (12), 7303–7318 (2007).

46. X. Zhang, *et al.*, Symmetry-breaking-induced nonlinear optics at a microcavity surface. *Nature Photonics* **13** (1), 21–24 (2019).